CRYSTAL GROWTH & DESIGN

pubs.acs.org/crystal

Article

Toward the Synthesis of New Zeolite Structures in the Presence of Cesium: Zeolite MMU-1

Published as part of a Crystal Growth and Design virtual special issue on Zeolite Crystal Engineering

Lubomira Tosheva,* Krassimir Garbev, Gary J. Miller, and Boriana Mihailova

Cite This: *Cryst. Growth Des.* 2023, 23, 3834−3844

Read Online

ACCESS | Metrics & More | Article Recommendations | Supporting Information

ABSTRACT: Nanosized small-pore zeolites RHO and MMU-1 (a new Cs-Na modification of an EDI-type zeolite structure) were prepared in the presence of cesium hydroxide by changing the molar composition of the precursor zeolite solution. XRD, Raman, and FTIR results indicated that Cs had a structure-directing effect and controlled the formation of the respective zeolite phases. The presence of water played a crucial role, and when the amount of water was under a certain level, the zeolite cancrinite was formed. Solvent-free syntheses were attempted, and the results confirmed the conclusions drawn based on the water-mediated syntheses, namely that both Cs and water determine the nature of the product formed. The structure of the new zeolite MMU-1 was resolved by Rietveld refinement. MMU-1 was found to exhibit tetragonal symmetry, space group $P\bar{4}2_1c$ (No. 114), and its framework is composed of four-membered and eight-membered TO_4-rings. The results reported suggest that there is the potential to synthesize other novel small-pore zeolite structures in the presence of cesium hydroxide by modifications of the chemical composition of the zeolite precursor solution.

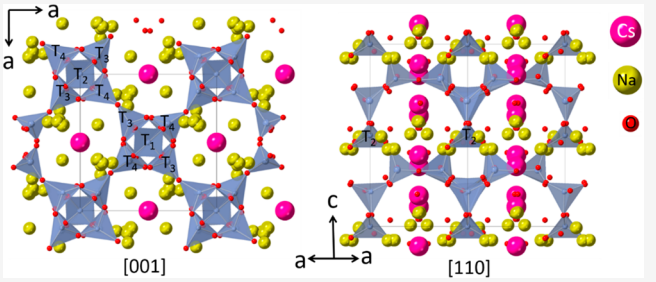

1. INTRODUCTION

Owing to their high external surface areas, enhanced selectivity, and longer catalyst lifetimes due to coke resistance, much attention has been paid to the development of more sustainable methods for the synthesis of nanosized zeolites. Stable colloidal suspensions of ultrasmall EMT and FAU nanozeolites have been prepared in the absence of organic structure-directing agents (OSDAs) in high yields by careful control of the zeolite precursor mixture and crystallization conditions.[1,2] Nanosized MFI and BEA zeolites have been synthesized by increasing the nutrient concentration in the starting gels containing reduced amounts of organic templates.[3] Solvent-free zeolite synthesis methods have been developed consisting of grinding together solid raw zeolite precursors, which contain traces of water, and the mixtures are converted into zeolites by heating.[4] The solvent-free methods generate less waste; however, the control over zeolite morphology is limited and the formation of nanozeolites by such methods has rarely been reported.[5] Despite the progress made in the synthesis of OSDA-free nanozeolites, the number of structures prepared remains limited and improvements of existing methods or modifications leading to the synthesis of new nanozeolite structures are highly desirable.[6]

Recently, small-pore eight-membered-ring zeolites have been attracting great research efforts due to their commercial application in important catalytic processes such as the NO_x removal from exhaust gases and the methanol-to-olefins conversion.[7] One of the most interesting members of this group of zeolites, particularly for CO_2 separation and capture applications, is zeolite RHO. The most mature technology for Postcombustion CO_2 Capture (PCC) is aqueous amine scrubbing, which is energy demanding and corrosive to equipment,[8] requiring an upgrade to more sustainable technologies in the transition to a net-zero-CO_2-emission society. Adsorption-based technologies are an attractive alternative. Zeolite RHO has shown great potential for use in such technologies because of its very high CO_2/CH_4 selectivity and high CO_2 adsorption capacity.[9] In addition, its flexible framework with tunable pore sizes depending on the extraframework cations offers additional control over its adsorption properties and "trapdoor" effects.[10−12] Other eight-membered-ring zeolites have also demonstrated potential for CO_2 adsorption applications, namely Zeolite-F,[13] MER,[14] and GIS.[15]

Nanosized zeolite RHO has recently been prepared in the absence of OSDAs.[16,17] The reported methods in these works

Received: February 28, 2023
Revised: April 12, 2023
Published: April 21, 2023

https://doi.org/10.1021/acs.cgd.3c00239
Cryst. Growth Des. 2023, 23, 3834−3844

Table 1. Silica Source and Molar Composition of the Synthesis Mixtures Used in This Study

	silica source	molar composition (water-mediated)
solution A	Ludox	10 SiO_2:0.77 Al_2O_3:7.9 Na_2O: 0.47Cs_2O:110 H_2O
solution B	geothermal silica	10 SiO_2:2.2 Al_2O_3:23 Na_2O:1.4 Cs_2O:383 H_2O
solution C	Ludox	10 SiO_2:2.2 Al_2O_3:23 Na_2O:1.4 Cs_2O:294 H_2O
solution D	Ludox	10 SiO_2:2.2 Al_2O_3:23 Na_2O:1.4 Cs_2O:383 H_2O
	silica source	molar composition (solvent-free)
mixture A	dried Ludox/geothermal silica	10 SiO_2:0.77 Al_2O_3:7.9 Na_2O:0.47Cs_2O:2 H_2O
mixture B	dried Ludox/geothermal silica	10 SiO_2:2.2 Al_2O_3:23 Na_2O:1.4 Cs_2O:5.7H_2O

have been adopted in the current work with the aim to prepare nanosized RHO and to study its formation mechanism by Raman and FTIR spectroscopy. More specifically, the role of Cs^+ and water in the structural characteristics of the product samples was studied in detail. Surprisingly, when the composition of the precursor mixture was modified by using a silica sol with a lower silica concentration, a new zeolite phase was repeatedly prepared. The structure of this new zeolite, zeolite MMU-1, was resolved by Rietveld refinement. An objective of this work was also to explore the application of solvent-free synthesis methods and to determine whether useful zeolite structures can be prepared, as well as to compare the characteristics of zeolites prepared by water-mediated and solvent-free synthesis methods.

2. EXPERIMENTAL SECTION

2.1. Materials. The following chemicals were used: Ludox HS-30 colloidal silica (Aldrich); Geo40 sol-UF2 (geothermal colloidal silica, 6 nm, 10.5 wt %, Geo 40 Limited); sodium aluminate ($NaAlO_2$) (50.5% Al_2O_3, 44.1% Na_2O, Fisher Scientific); sodium hydroxide (NaOH) pellets (analytical reagent grade, Fisher Scientific); cesium hydroxide hydrate ($CsOH{\cdot}xH_2O$) (99.9%, 15−20% H_2O, Alfa Aesar). The colloidal silica suspensions were dried at 80 °C overnight and ground prior to use in the solvent-free syntheses.

2.2. Water-Mediated Zeolite Synthesis. Zeolite RHO was synthesized according to reference (16) with some modifications. First, 1.03 g of $NaAlO_2$ was dissolved in 3.67 g of distilled water in a beaker with stirring. The beaker was placed in a large Petri dish with cold tap water to keep the temperature constant upon the addition of 3.64 g of NaOH and 1.18 g of $CsOH{\cdot}xH_2O$. The mixture was stirred until dissolution of the hydroxides, and then 13.34 g of Ludox was added dropwise. This synthesis solution will be referred to as solution A in the text, and its molar composition is given in Table 1.

The same synthesis was repeated but using the geothermal silica instead of Ludox. The lower silica concentration in the geothermal silica compared to Ludox (10.5 wt % vs 30.0 wt %) resulted in a solution with the molar composition given in Table 1 (solution B). Solutions A and B were both stirred for 4 h, transferred to 150 mL polypropylene reactors, and hydrothermally treated at 80 °C for 15 h. After the treatment, the milky suspensions obtained were purified with ca. 350 mL of distilled water by four times of centrifugation and redispersion in distilled water. The purified samples were dried at 80 °C overnight. Precursor-zeolite samples (Pre-zeolite) were prepared by purifying and drying the aged solutions A and B prior to subjecting to hydrothermal treatment.

The influence of the type of silica sol used was further studied using Ludox and (i) adding 4.66 g of Ludox to match the SiO_2 content of the geothermal silica and keeping all other parameters the same (solution C in Table 1) and (ii) adding 4.66 g of Ludox and 8.68 g of distilled water to match both the SiO_2 and water content of the geothermal silica (solution D in Table 1).

The influence of the presence of cesium hydroxide was also studied, and two samples were prepared in exactly the same way as described for solutions A and B but without the addition of $CsOH{\cdot}xH_2O$.

2.3. Solvent-Free Synthesis. A series of experiments was also performed using dried silica sols and without the addition of any distilled water. In these experiments, the same silica content as in solutions A and B (4 or 1.4 g, respectively) was used with both silica sources. The dried silica sols were manually ground in a mortar for 5 min with 1.03 g of $NaAlO_2$, 3.64 g of NaOH, and 1.18 g of $CsOH{\cdot}xH_2O$. The molar compositions of the corresponding two mixtures, mixture A (4 g silica) and mixture B (1.4 g silica), are given in Table 1. Traces of water come from the use of $CsOH{\cdot}xH_2O$. The solid mixtures were transferred to 150 mL polypropylene reactors and treated at 80 °C for periods of time between 20 h and 7 d. In some experiments, the polypropylene reactors were transferred to an oven after 4 h of static aging under ambient conditions. After the treatment, the samples were purified and dried as described before. The influence of the presence of cesium hydroxide was also studied, and a sample was prepared in exactly the same way as described using 4 g of dry Ludox but without the addition of $CsOH{\cdot}xH_2O$. Precursor samples were also prepared for the solvent-free synthesis using 4 g of Ludox, namely sample MM (mechanical mixture), which was prepared by purifying the ground reagents prior to heating, and sample "heated MM", which was prepared by heating the ground reagents (using 4 g of Ludox) for 20 h at 80 °C followed by purification.

2.4. Characterization Methods. X-ray diffraction (XRD) data were collected on a PANalytical X'pert Powder X-ray diffractometer using Cu Kα_1 radiation (λ = 1.5406 Å) with generator settings of 45 kV and 40 mA. Automatic divergence and antiscatter slits were used on the incident and diffracted beam paths with data collected using a PIXCel 1-D detector operating in scanning line mode with an active length of 3.347° 2θ. The incident beam was passed through a 10 mm beam mask with the automatic divergence slits on the source set to maintain a constant irradiated length of 5 mm throughout the scan. The automatic antiscatter slits on the detector were also set to maintain a constant 5 mm aperture. Data were collected in the range 10−140° 2θ with a step size of 0.013° 2θ and a measuring time of 89 s per step. The samples were rotated at 60 rpm during the data collection. Phase identification was performed using the search-match function in HighScore Plus v. 4.8 (PANalytical, 2018) against the Crystallography Open Database derived search-match database.[18] Crystallite sizes were determined using the Size/Strain calculator incorporated into PANalytical Data Viewer (PANalytical B.V, 2011) with the instrumental broadening function determined using a NIST SRM674b CeO_2 external standard.

X-ray fluorescence (XRF) data were collected using a Rigaku NEX-CG energy-dispersive X-ray fluorescence spectrometer. For emission of primary radiation an X-ray tube (I_{max}= 2 mA, V_{max}= 50 kV) with a 50 W Pd anode was used. The secondary targets, voltage, and time used were Mo 50 kV and 100 s, Cu 50 kV and 100 s, RX9 25 kV and 100 s, and Si 25 kV and 300 s with the tube current set automatically in all cases. The samples were presented as loose powders and analyzed under a helium purge with semiquantitative results calculated using the Rigaku Profile Fitting-Spectra Quant X (RPF-SQX) Fundamental Parameters program (Rigaku, 2007, NEX-CG Software v3.42).

Scanning electron microscopy (SEM) images were obtained with a Carl Zeiss Supra 40 V scanning electron microscope. Samples were sputtered with gold prior to analysis. Nitrogen adsorption isotherm measurements at −196 °C were performed with a Micrometrics ASAP 2020 surface area analyzer. Samples were degassed at 300 °C

https://doi.org/10.1021/acs.cgd.3c00239
Cryst. Growth Des. 2023, 23, 3834−3844

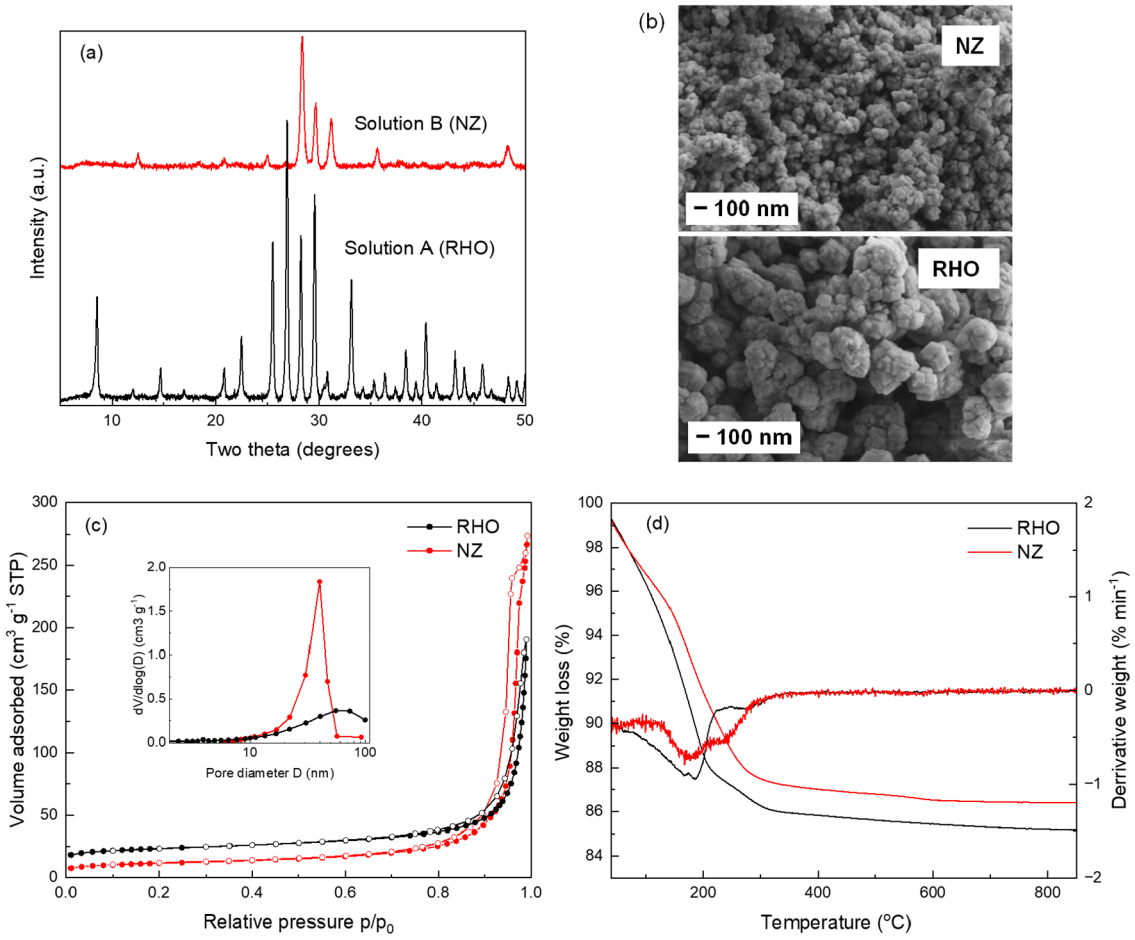

Figure 1. (a) XRD patterns of the samples prepared from solutions A and B and the corresponding (b) SEM images, (c) nitrogen adsorption−desorption isotherms and (insert) pore-size distributions, and (d) thermal analysis curves.

overnight prior to analysis. Surface areas were calculated using the Brunauer−Emmett−Teller (BET) method, whereas Barrett−Joyner−Halenda (BJH) pore size distributions were determined from the desorption branch of the isotherms. Micropore volumes and external surface areas were determined by the *t*-plot method. Total pore volumes were calculated from the volume adsorbed at a relative pressure of 0.99. Thermogravimetric analysis (TGA) was performed with a TGA4000 instrument from PerkinElmer. Samples were heated to 900 °C at a heating rate of 10 °C min^{-1} under air.

Raman spectra of the final and intermediate products of synthesis as well as of the dried silica sources were collected with a Horiba T64000 triple-monochromator spectrometer equipped with a LN_2-cooled CCD detector and an Olympus BX41 confocal microscope in the spectral range 15−3800 cm^{-1}. The spectra were excited with the green line (λ = 514.532 nm) of a Coherent Innova 90C FreD Ar^+ laser, using a 50× objective and a 500 μm confocal hole. The laser spot and power on the sample surface were ∼2 μm and 7.9 mW, respectively, which were sufficient to avoid any sample damage under the laser radiation, as revealed by test measurements with a lower surface laser power. The Raman spectrometer was calibrated to the 520.5 cm^{-1} peak of a silicon wafer. The instrumental precision in the peak positions was 0.35 cm^{-1}, while the achieved spectral resolution was 2 cm^{-1}. Fourier transform infrared (FTIR) spectra from the same series of samples were collected with a Bruker Vertex 70 FTIR spectrometer equipped with an RT-DLaTGS detector, using the KBr-pellet technique and an instrumental resolution of 2 cm^{-1}. The FTIR spectra were corrected for atmospheric water and CO_2 via the OPUS 7.5 software, whereas both Raman and FTIR spectra were temperature reduced, using the relation $I_{\text{rreduced}} = \frac{I_{\text{measured}}}{n(\omega,T)+1}$, where I is the intensity and $n(\omega,T)$ is the Bose−Einstein occupation factor $n(\omega, T) = \frac{1}{e^{\hbar\omega/k_B T}-1}$ with $\hbar$ designating the reduced Planck's constant, k_B the Boltzmann constant, T the room temperature (in K), and ω the phonon angular frequency (in s^{-1}). The latter correction slightly modified the spectral-peak intensities below 400 cm^{-1} but not the peak positions.

2.5. Atomic-Structure Determination of the Zeolite Prepared from Solution B. For the purpose of atomic-structure refinements, a powder pattern of the sample prepared from solution B was taken on an Empyrean diffractometer operated at 1600 W (40 kW × 40 mA). A fixed divergence slit of 1/8° combined with 1/2° antiscattering slit, 0.02 rad Soller slits, 4 mm mask, and PIXcel 3D detector were used for maximal angular resolution. The XRD pattern was indexed with the McMail routine implemented in HighScore Plus v.5. The possible space groups resulting from the indexing were checked by the WPPD methods of Pawley and Le Bail implemented in TOPAS v.6 (Bruker-AXS, Karlsruhe, Germany). The consequent analyses with charge flipping and Rietveld refinements were also conducted with TOPAS v.6.

3. RESULTS AND DISCUSSION

3.1. Water-Mediated Zeolite Synthesis. Initial experiments were performed using solutions A and B (Figure 1). As expected, synthesis from solution A resulted in an RHO-type zeolite in accordance with previous studies (Figure 1a).[16] The sample was composed of 50−100 nm primary nanocrystals, which were further arranged into 300−500 nm larger aggregates (Figure 1b). Synthesis from solution B resulted in

https://doi.org/10.1021/acs.cgd.3c00239
Cryst. Growth Des. 2023, 23, 3834−3844

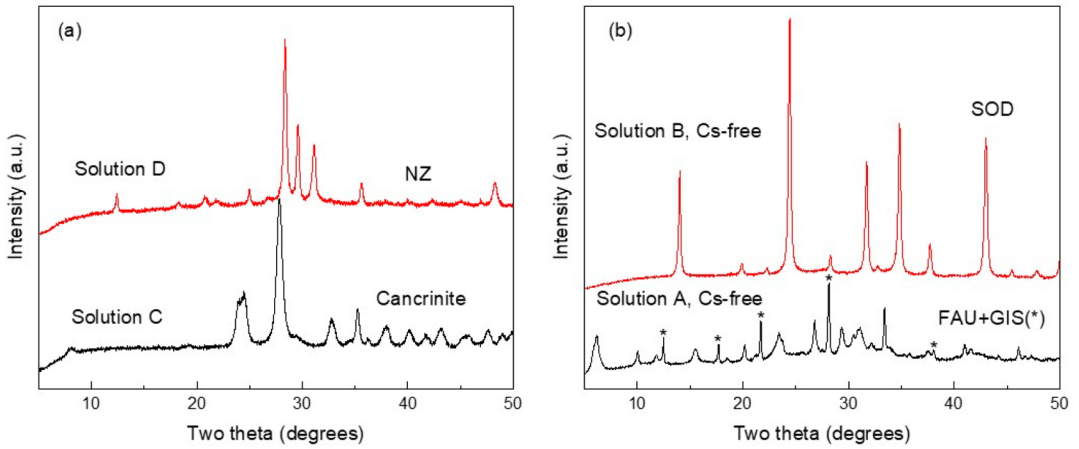

Figure 2. XRD patterns of (a) samples prepared from solution C and solution D and (b) samples prepared from solutions A and B without the addition of cesium hydroxide.

Table 2. Si/Al and Cs/Si Ratios (Ratios Calculated Using Element wt % XRF Data) and Textural Characteristics (BET Areas, S_{BET}; Micropore Volumes, V_{μ}; External Areas, S_{EXT}; Total Pore Volumes, V_{TOTAL}; Crystallite Sizes) of the Different Zeolite Structures Prepared from Solutions A–D

solution	zeolite	Si/Al	Cs/Si	S_{BET} ($m^2\ g^{-1}$)	V_{μ} ($cm^3\ g^{-1}$)	S_{EXT} ($m^2\ g^{-1}$)	V_{TOTAL} ($cm^3\ g^{-1}$)	crystallite size (Å)
A	RHO	1.48	0.65	79	0.020	37	0.29	553
B	NZ	1.09	1.33	40	0.005	29	0.41	323
C	cancrinite	1.14	1.08	51	0.002	47	0.45	297
D	NZ	1.22	1.19	42	0.008	25	0.43	374

a crystalline zeolite-like sample, for which the XRD pattern did not match any existing structures, and for now, this structure will be labeled as NZ (new zeolite) (Figure 1a). The synthesis was reproduced several times, and consistent XRD results were obtained. Sample NZ composed of nanoparticles with sizes of between 20 and 40 nm (Figure 1b). The nitrogen adsorption isotherms indicated that the zeolite pore structures of both samples were largely inaccessible to the nitrogen molecule, which in the case of RHO could be related to blockage of their eight-membered-ring openings by cations (Figure 1c).[16] A hysteresis was observed at high relative pressures for both samples because of interparticle mesoporosity associated with their nanosized nature, which was more pronounced for NZ in accordance with the SEM results. The pore-size distributions indicated a narrower distribution of mesopores for NZ (10–60 nm) compared to RHO (10 to >100 nm) as a result of the different morphology of the samples. Finally, the different zeolite structures resulted in differences in the TGA curves. NZ showed a weight loss of 13 wt % at 300 °C, which was lower compared to the weight loss for RHO (14 wt %). In addition, the DTA curve indicated the presence of two types of water in NZ (Figure 1d).

Solutions A and B were prepared with two different silica sols with two different concentrations. The role of the silica source and concentration were further verified using the Ludox colloidal silica source by performing experiments with solution C (to match the silica concentration of solution B but without addition of extra distilled water, Table 1) and with solution D (to match both the silica concentration and water content of solution B, Table 1). XRD analysis showed that the synthesis performed using solution C resulted in cancrinite, whereas solution D yielded NZ (Figure 2a). These results indicate that (i) NZ can be synthesized with both silica sources as long as the molar composition of the synthesis solution is the same and (ii) the presence of a minimal amount of water seems essential for the synthesis of NZ; less water results in the synthesis of cancrinite. Further characteristics of the cancrinite zeolite prepared from solution C are provided in Figure S1. The sample was composed of fine nanoparticles, and its isotherm resembled the isotherm of NZ. A detailed comparison between NZ prepared from solution A (geothermal silica) and solution D (Ludox) is shown in Figure S2. The results indicate subtle differences in morphology and textural porosity between the two samples as a result of the use of different silica sources.

Data about the chemical composition and textural characteristics of the samples prepared from solutions A–D are provided in Table 2. Zeolite RHO had a higher Si/Al ratio and lower Cs/Si ratio compared to all other samples, which could be explained by the differences in the molar compositions of the synthesis solutions. This sample had the lowest total pore volume and largest crystallite size as well, in accordance with the sample's morphology according to SEM.

Finally, the role of the presence of cesium was evaluated by performing synthesis from Cs-free solutions A and B. Figure 2b indicates that a mixture of FAU- and GIS-type zeolites crystallizes from the Cs-free solution A, whereas SOD-type zeolite is formed from the Cs-free solution B, in agreement with previous studies.[19] These results demonstrate the structure-directing role of Cs in the formation of RHO and NZ zeolites.

The Raman and FTIR spectra of RHO (prepared from solution A) and NZ (prepared from solution B) along with the spectra of the corresponding precursors and silica sources are shown in Figure 3. As can be seen, both zeolites show a strong Raman peak near 520 cm^{-1}, indicating four-membered TO_4 rings in both frameworks.[20−22] The difference in the Raman peak position, however, implies different ring geometries in NZ

https://doi.org/10.1021/acs.cgd.3c00239
Cryst. Growth Des. 2023, 23, 3834−3844

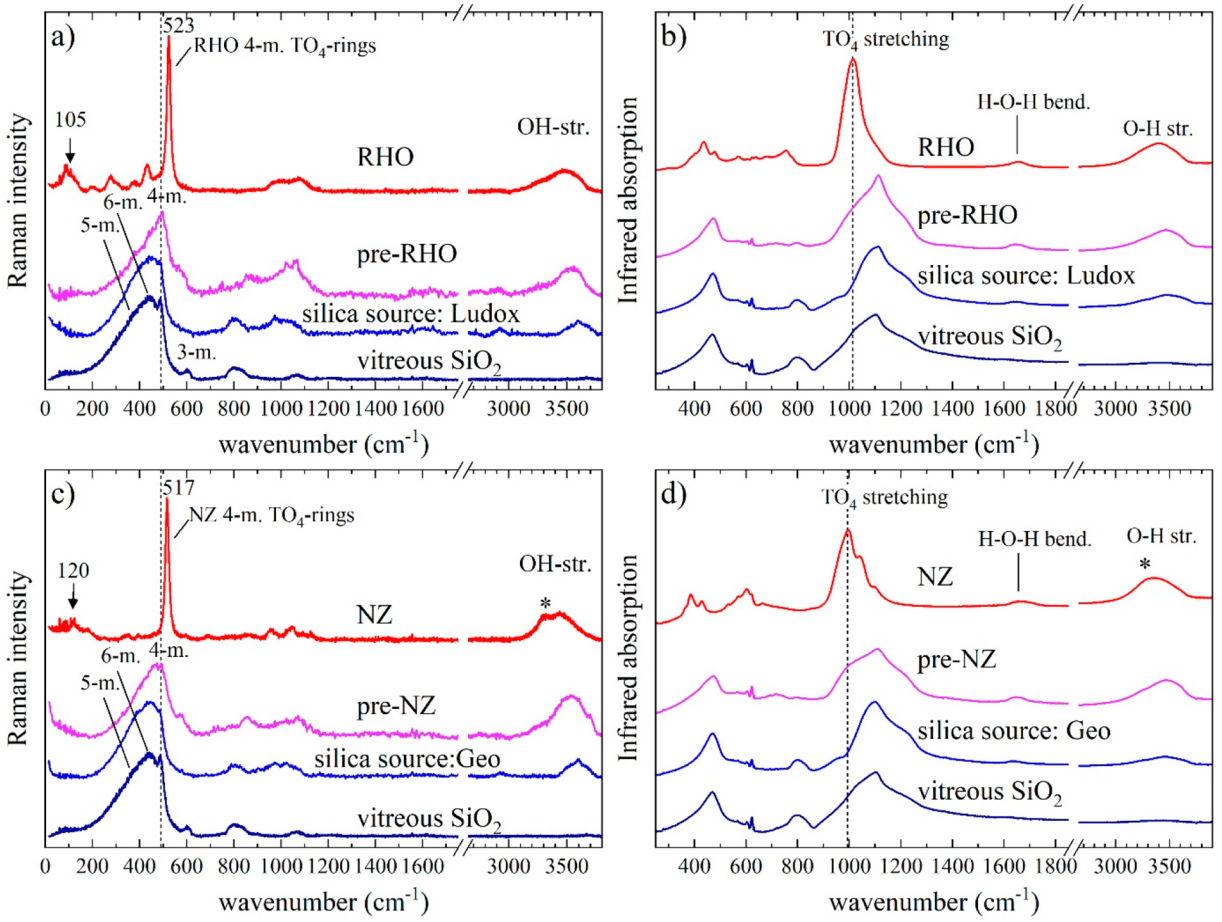

Figure 3. (a, c) Raman and (b, d) FTIR spectra of RHO and NZ, the corresponding precursors (pre-RHO and pre-NZ), and dried silica sources (Ludox and Geo). Spectra of commercial vitreous silica (Suprasil) have also been included in the figures as a reference of amorphous silica. The asterisks in (c) and (d) denote the extra signal in the OH-stretching range observed for NZ.

and RHO. Moreover, NZ exhibits a better-resolved subpeak structure of the infrared TO_4-stretching peak compared to RHO, suggesting variations in the T−O bonds, i.e. more distorted TO_4 tetrahedra in NZ than in RHO. Besides, for NZ there is an additional Raman scattering as well as IR absorption signal to the main OH-stretching peak, which indicates an abundant second type of hydrous species in this zeolite, in accordance with the TGA results.

The Raman and IR spectra do not reveal any short-range or intermediate-range structural difference between the two silica sources, emphasizing again that the different crystalline structures of the final products stem from the different chemistries of the solutions. However, the structure of both silica sources slightly differs from that of silica glass by the absence of three-membered TO_4-rings (no Raman peak near 606 cm^{-1}) and a smaller amount of four-membered rings (weaker Raman scattering near 498 cm^{-1}). Besides, both Raman and FTIR spectra reveal incorporated H_2O in the amorphous silica source. Even prior to any hydrothermal treatment, the TO_4-network further changes when mixing the silica source with the other additives. The additional lower-energy TO_4-stretching peak (near 1000 cm^{-1}) in the FTIR spectra of the precursors matches very well the strongest FTIR peak of the corresponding zeolite structure, indicating initial incorporation of Al into the TO_4-network. This also conforms with the increasing content of hydrous species, revealed by the enhanced O−H stretching signal in both the Raman and FTIR spectra of the precursors in comparison with the spectra of the silica sources. The Raman spectra of the precursors also indicate reinforcement of the four-membered TO_4-rings relative to the five- and six-membered rings. This is more pronounced for the RHO-precursor than for the NZ-precursor. Yet, the four-membered rings in the precursors have different geometry compared to the 4-ring geometry in the corresponding zeolite framework: that is, a hydrothermal treatment is necessary for the formation of intermediate-range order typical of the corresponding crystalline phase. Recently, it was proposed that the Raman peak positions are in fact related to the types of zeolite tricycle bridges formed by three rings sharing the same T−O−T bridge, with the primary importance of the smallest ring in the tricycle.[22] It was also shown that for pure-silica frameworks the strongest Raman peak shifts toward lower wavenumbers with the increase in the Si−O−Si angle averaged over the existing tricycles containing the smallest-size ring.[22] The comparison between different zeolites containing four-membered rings (Figure 4) suggests that the average T−O−T angle for NZ is larger than that for RHO but smaller than those for CAN, FAU, and LTA; note that the Raman peak position between 480 and 530 cm^{-1} does not show any correlation with the Si/Al ratio, indicating that it reflects mainly the geometrical difference in the ring tricycles in the zeolite frameworks.

https://doi.org/10.1021/acs.cgd.3c00239
Cryst. Growth Des. 2023, 23, 3834−3844

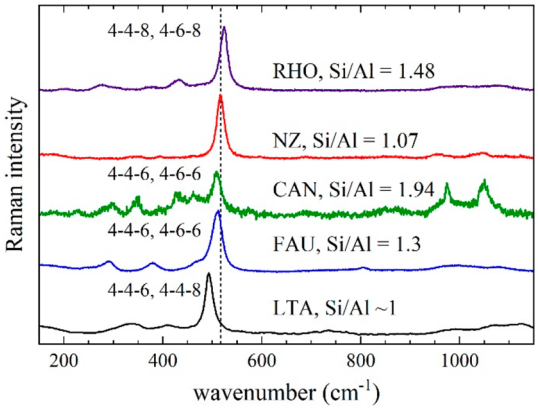

Figure 4. Comparison between Raman spectra of various zeolites containing four-membered rings within tricycle bridges of four-, six-, and eight-membered rings, as specified in the plot.

3.2. Solvent-Free Synthesis. Numerous experiments were performed to explore the possibility for solvent-free synthesis, in which the colloidal silica sol used to prepare solutions A and B was dried prior to use. Although the results were not highly reproducible in terms of crystallinity or chemical composition, probably because of the manual mixing of the solid compounds and their nature, some trends could be drawn from these experiments. The samples prepared using 1.4 g of silica were always amorphous, independent of the silica source/treatment time used. For the samples prepared using 4 g of silica, differences were observed in the samples' crystallinity and chemical composition depending on the silica source, although the differences could also be related to the poor reproducibility of the results. Figure 5 shows results obtained for the samples prepared from the solvent-free synthesis using the two silica sources after 7 days of treatment. Cancrinite was formed in the presence of both silica sources (Figure 5a). Some differences in the textural characteristics of the samples and their morphology were observed, which could be attributed to the different silica sources used (Figure 5b,c). The cancrinite sample prepared from solution C was also included in this figure for a comparison. As can be seen, the particle size of the latter sample was smaller compared to those of the solvent-free samples, with a significantly higher pore volume (Figure 5 and Table 3).

The sample prepared using 4 g of dried Ludox in the absence of Cs for 7 d of treatment was amorphous, indicating that Cs has a structure-directing role in the solvent-free synthesis as well. The Si/Al ratio of this sample was 2.86, suggesting that Cs promotes the Al incorporation into the zeolite structure.

According to Raman and FTIR spectroscopy, the mechanical mixture (MM) for the solvent-free synthesis using 4 g of silica shows similar differences with respect to the silica source as the precursors do in the case of water-mediated zeolite synthesis: a slight decrease of the fraction of five- and six-membered rings with respect to the amount of four-membered rings (see Figure 6a) and a weak additional lower-wavenumber IR absorption next to the main peak generated by TO_4 stretching (Figure 5b) The heating of MM leads to further suppression of the five- and six-membered rings typical of silica glass and changes the geometry of the four-membered rings. However, the comparison with the CAN samples formed after 7 d of heating at 80 °C reveals that the intermediate-range structure of heated MM mimics that of CAN. This further emphasizes the crucial role of the amount of water present in the system for the resultant zeolite framework structure.

3.3. Structure Refinement of NZ. *3.3.1. Chemical Formula.* The chemical formula calculated from the elemental analysis results in $Na_{0.38}Cs_{0.12}Si_{0.49}Al_{0.48}V_{0.02}Ti_{0.01}O_2$ based on 2 oxygens and considering V in a 3 valence state. The weight loss of the NZ sample measured by TGA is 13 wt %, resulting in 0.7 H_2O molecules considering the formula above. Traces of V and Ti are from impurities in reagents used to prepare solution B.

3.3.2. Structure of NZ. The powder pattern of NZ resembles that of $CsAlSiO_4 \cdot H_2O$ described by Kosurkov and Nadel (ICSD 039-0131), matching all strong reflections, but not the weaker ones.[23] The authors point to a possible body-centered tetragonal space group. Much better matching is achieved by ICSD 39-0217, describing the powder pattern of Zeolite F with the nominal formula $Na_5Al_5Si_5O_{20} \cdot 9H_2O$ and Z

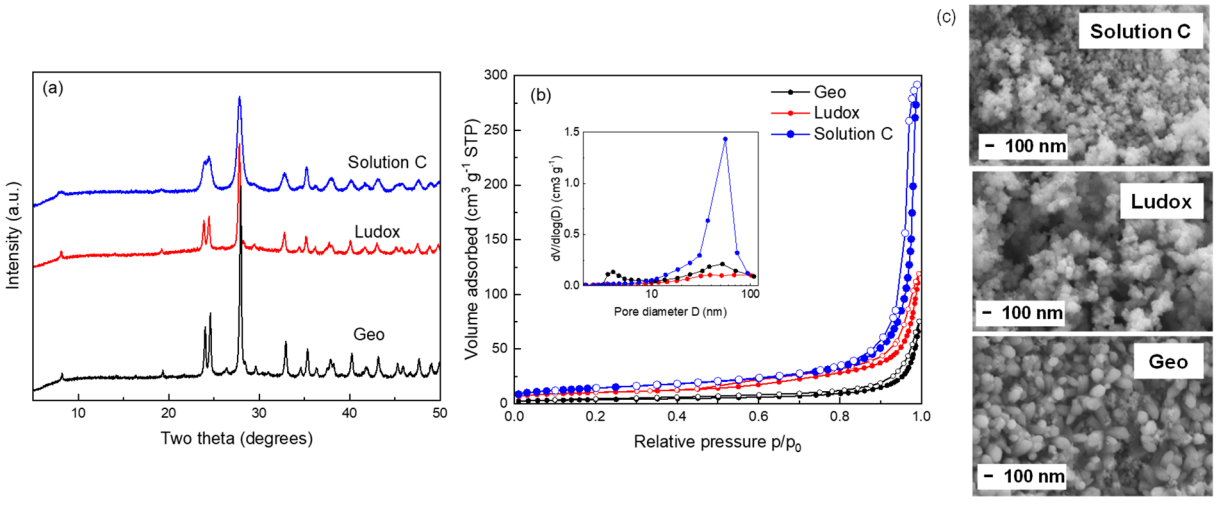

Figure 5. (a) XRD patterns of the samples prepared from solvent-free synthesis using 4 g of Ludox (Ludox) or geothermal silica (Geo), (b) nitrogen adsorption−desorption isotherms and (insert) pore-size distributions, and (c) SEM images. Corresponding results for the synthesis from solution C are included for a comparison.

https://doi.org/10.1021/acs.cgd.3c00239
Cryst. Growth Des. 2023, 23, 3834−3844

Table 3. Si/Al and Cs/Si Ratios (Ratios Calculated Using Element wt % XRF Data) and Textural Characteristics (BET Areas, S_{BET}; Micropore Volumes, V_{μ}; External Areas, S_{EXT}; Total Pore Volumes, V_{TOTAL}; Crystallite Sizes) of the Different Cancrinite Zeolite Structures Prepared Using Dried Geothermal Silica (Geo), Dried Ludox (Ludox), and Solution C

sample	Si/Al	Cs/Si	S_{BET} ($m^2\ g^{-1}$)	V_{μ} ($cm^3\ g^{-1}$)	S_{EXT} ($m^2\ g^{-1}$)	V_{TOTAL} ($cm^3\ g^{-1}$)	crystallite size (Å)
Geo	1.19	0.88	13	0.0002	12	0.10	482
Ludox	1.94	0.56	35	0.0039	27	0.17	376
solution C	1.14	1.08	51	0.0015	47	0.45	297

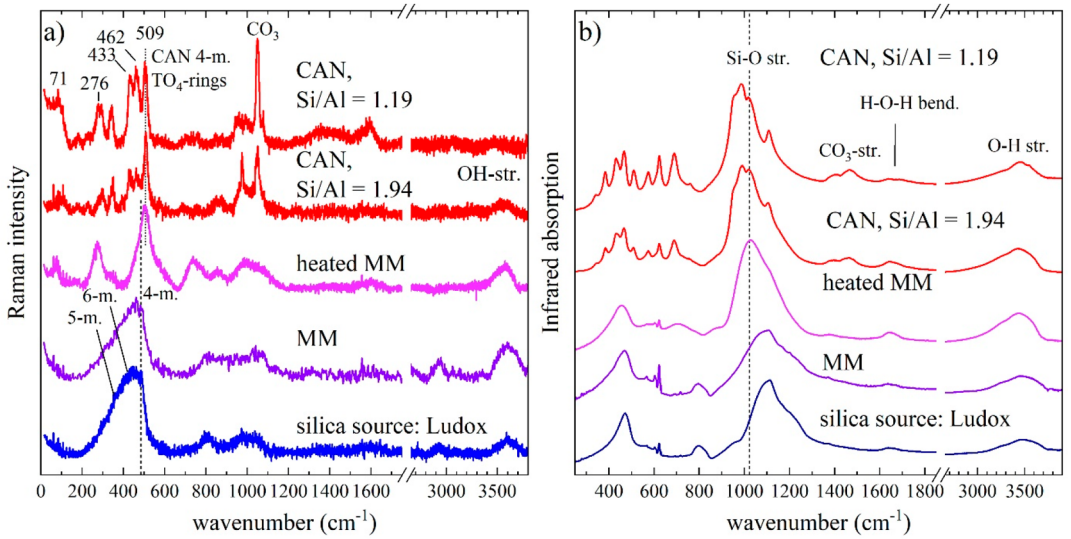

Figure 6. Raman (a) and IR spectra (b) of the silica source, mechanical mixture (MM), and heated MM in solvent-free zeolite synthesis, along with the spectra of CAN samples obtained after 7 days of heating at 80 °C.

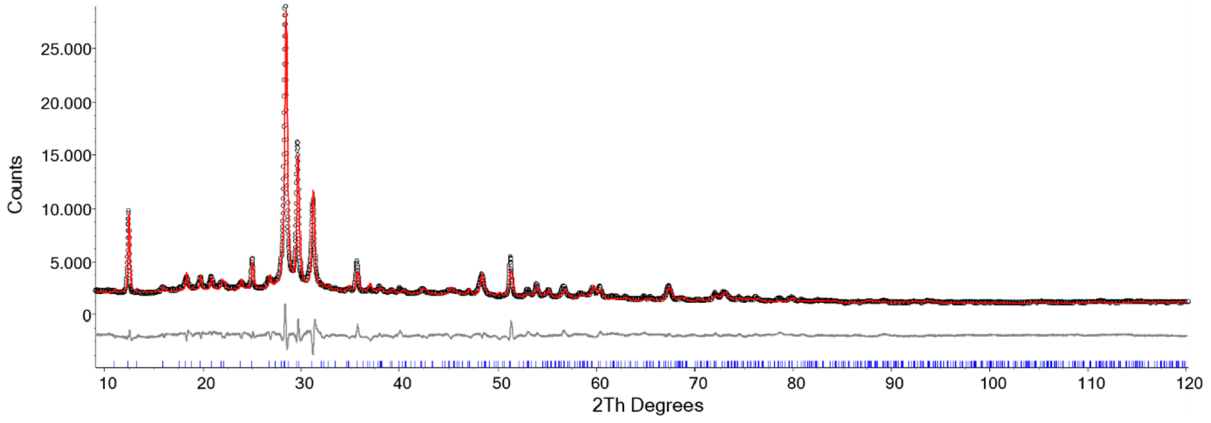

Figure 7. Rietveld plot of the structure refinement of NZ.

= 1. Expanding the chemical composition of sample NZ to this formula results in $(Na_{3.8}Cs_{1.2})[Si_{4.9}Al_{4.8}V_{0.2}Ti_{0.1}O_{20}]\cdot 7H_2O$. Baerlocher and Barker solved the structure of zeolite F in space group (SG) No. 113 $P\bar{4}2_1m$ but pointed to the presence of pseudosymmetry due to disorder, suggesting that the real symmetry must be lower.[24] Thus, as a first step to solve the structure of NZ, a Le Bail fit was performed with an *hkl* phase based on $P\bar{4}2_1m$ with the unit cell parameters proposed by Barlocher and Barker: a = 10.056 Å, c = 6.68 Å. The refinement resulted in a = 10.067 Å and c = 6.650 Å, but leaving the prominent peak at 4.26 Å (20.83· 2θ) and those with lower intensity around 22° 2θ and between 10 and 12° 2θ largely unfitted. In a further step, a possible doubling of the c unit-cell parameter was taken into account and several Le Bail fit trials were performed considering different space groups. Best results were obtained with both "klassengleiche" subgroups with index 2: $P\bar{4}2_1m$ (SG No. 113) and $P\bar{4}2_1c$ (SG No. 114) with a = 10.067 Å and c = 13.299 Å. The reflection with d = 4.26 Å was fitted as stemming from (211). A Pawley fit was performed to extract the *hkl* intensities in the 2θ range between 8 and 120° for the purpose of the charge-flipping procedure implemented in TOPAS 6. According to the chemical analysis, 9.6 Al, 9.8 Si, 0.2 V, 0.1 Ti, 7.6 Na, 2.4 Cs, and 54 O atoms were introduced in the doubled unit cell (Z = 2). As the increasing number perturbations did not lead to significant results, the parameters were gradually varied by introducing Ramp macros. Constraints such as extending of the Ewald sphere and excluding the reflections with low d values (<1.1 Å) were imposed along the use of a diagonally normalized A matrix (D) combined with the tangent formula

https://doi.org/10.1021/acs.cgd.3c00239
Cryst. Growth Des. 2023, 23, 3834−3844

Table 4. Results from the Structure Refinement[a]

symmetry: tetragonal, space group H-M: $P\bar{4}2_1c$ (No. 114)
lattice parameters: a = 10.085(7) Å, b = 10.085(7) Å, c = 13.326(9) Å, $\alpha = \beta = \gamma = 90°$
formula: $(Cs_{1.17}Na_{3.69})[Si_{5.14}Al_{4.86}O_{20}]\cdot 7H_2O$
cell volume: 1355(2) Å^3,; Z = 2; density 2.581 g cm^{-3}
background: Chebyshev 6th-order polynomial
preferred orientation: March−Dollase 110 and 100
crystal size double-Voigt approach: 80(4) nm
criteria of fit: R_{Bragg} 2.003; R_{exp} 2.241; R_{wp} 6.489; R_p 4.962; DWS 0.4; GOF 2.89

site	atom	mult	x	y	z	occ	B_{eq}
T1	Al+3	2	0	0	0	0.49	0.7
T1	Si+4	2	0	0	0	0.51	0.7
T2	Al+3	2	0.5	0.5	0	0.49	0.68
T2	Si+4	2	0.5	0.5	0	0.51	0.68
T3	Al+3	8	0.1333(18)	0.1258(16)	0.1908(14)	0.49	1
T3	Si+4	8	0.1333(18)	0.1258(16)	0.1908(14)	0.51	1
T4	Al+3	8	0.3642(18)	0.6416(15)	0.8103(13)	0.49	1
T4	Si+4	8	0.3642(18)	0.6416(15)	0.8103(13)	0.51	1
O1	O-2	8	0.105(3)	0.089(3)	0.0620(18)	1	1
O12	O-2	8	0.403(4)	0.608(4)	0.9345(19)	1	1
O2	O-2	8	0.976(3)	0.181(4)	0.231(2)	1	1
O22	O-2	8	0.487(4)	0.683(4)	0.741(2)	1	1
O3	O-2	8	0.224(3)	0.276(3)	0.1963(15)	1	1
A1	Na+1	8	0.150(3)	0.265(3)	0.493(2)	0.21(7)	1
A1	Cs+1	8	0.150(3)	0.265(3)	0.493(2)	0.02(1)	1
A2	Na+1	8	0.870(3)	0.371(3)	0.0749(16)	0.21(7)	1
A2	Cs+1	8	0.870(3)	0.371(3)	0.0749(16)	0.03(1)	1
O10	O-2	8	0.870(3)	0.371(3)	0.075(2)	0.25(3)	1
A3	Cs+1	4	0	0.5	0.169(1)	0.25(4)	1
A4	Na+1	8	0.152(2)	0.335(2)	0.423(5)	0.25(3)	1
O11	O-2	8	0.152(2)	0.335(2)	0.423(5)	0.25(6)	1
A5	Na+1	8	0.122(2)	0.371(2)	0.425(4)	0.25(4)	1
A5	O-2	8	0.122(2)	0.371(2)	0.425(4)	0.25(7)	1
A6	Cs+1	4	0	0.5	0.3914(12)	0.25(4)	1
O4	O-2	8	0.276(6)	0.233(6)	0.460(4)	0.25	1
O6	O-2	8	−0.120(6)	0.396(7)	0.177(3)	0.25	1
O8	O-2	8	0.024(7)	0.295(6)	0.465(5)	0.25	1
O9	O-2	8	−0.175(6)	0.554(9)	0.405(4)	0.25	1

[a]Estimated standard deviations are given in parentheses.

Table 5. Coordination of the Tetrahedral Sites[a]

T1		T2		T3		T4	
O1	1.615 ± 0.029	O12	1.704 ± 0.037	O2	1.764 ± 0.042	O2	1.65 ± 0.03
O1	1.615 ± 0.029	O12	1.704 ± 0.037	O22	1.630 ± 0.042	O3	1.62 ± 0.03
O1	1.615 ± 0.029	O12	1.704 ± 0.037	O1	1.779 ± 0.030	O12	1.73 ± 0.03
O1	1.615 ± 0.029	O12	1.704 ± 0.037	O3	1.771 ± 0.035	O22	1.60 ± 0.04

[a]Interatomic distances are given in Å.

in order to account for powder data.[25] The best R factor obtained was 0.26. The positions of the Si(Al) atoms were successfully identified along with these of the Cs atoms (Supporting Information). Four-membered (4M) and eight-membered (8M) rings of tetrahedra were identified as themain structural units and Cs was localized in the vicinity of the 8M rings, similar to other Cs-containing zeolites.[26,27]

For the purposes of the Rietveld refinement a starting model based on the results from the charge-flipping method and on the modified structure of Zeolite F (ICSD 6272) by transforming it in space group No. 114 and doubling the c unit cell parameter as suggested from the WPPD methods. The occupancy of the mixed positions was changed to fit the chemical composition derived from XRF within uncertainties. A detailed description of the fitting procedure is given in the Supporting Information.

The presence of Ti could be neglected in the structure refinements, while a small amount of 5-valence V could be adopted to the tetrahedral sites. Alternatively, 3-valence V could be at the octahedral site, without affecting the structure refinement. Given the minimal amounts of both Ti and V, coming from unavoidable impurities in the oxides used in the synthesis mixture, we can suggest a nominal chemical formula of $(Cs_{1.17}Na_{3.69})[Si_{5.14}Al_{4.86}O_{20}]\cdot 7H_2O$. The Rietveld plot and

https://doi.org/10.1021/acs.cgd.3c00239
Cryst. Growth Des. 2023, 23, 3834−3844

the final results are given in Figure 7 and Table 4, respectively. Note that the precise localization of the oxygen atoms from H_2O in the pores, combined with the split model for the distribution of Na, was challenging and might need further neutron diffraction experiments. The coordinating oxygen atoms of the four tetrahedral sites (T1−T4) and the corresponding bond lengths are given in Table 5. The site T1 (0,0,0) is maximally constrained and coordinated by O1. Therefore, this tetrahedron is not distorted, similarly to T2 (0.5,0.5,0). However, T3 and T4 (especially T3) seem to be rather distorted with some bond lengths well beyond 1.7 Å, in full agreement with the resolved substructure of the SiO_4 stretching peak in the FTIR spectrum of NZ.

The main structural units of NZ consist of 4M and 8M rings, the latter running along both [001] and [110] (Figure 8). The

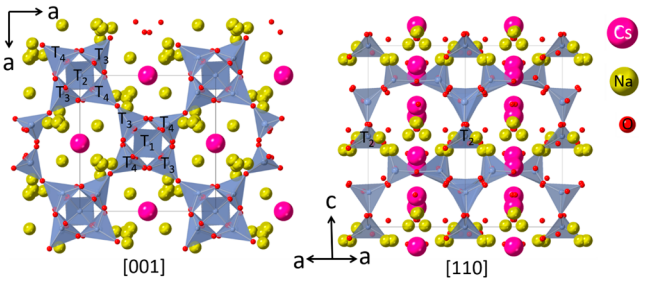

Figure 8. Structure of NZ seen along [001] (left) and along [110] (right).

4M and 8M rings form 8-4-4 tricycle bridges with a mean value of the T−O−T bond angle of 139.5°, which corroborates well the relatively high position (~517 cm^{-1}) of the strongest Raman peak (see Figure 4), following the general trend of zeolite frameworks comprising four-membered rings.[22] The geometrical diameter of the 8M rings (the distance between opposite O atoms) is within the range 6.4−7.9 Å. The alkali cations are distributed in the vicinity of the 8M rings with Cs preferentially occupying the center of the cavities. The distribution of Na seems to be quite complicated due to split positions. It should be emphasized that the presence of two types on cationic modifiers (Na, Cs) should result in different interactions between the modifiers and the surrounding water molecules, which explains the existence of two O−H stretching peaks in the Raman and IR spectra of NZ (see Figure 3c,d). The presence of two rather different H_2O environments underlines the role of water molecules for the formation of the new channel structure. The authors have assigned the NZ the name MMU-1 (a new Cs-Na modification of an EDI-type zeolite structure).

Figure 9 compares the TO_4 framework of NZ with that of zeolite F (ICSD 6772, chemical composition $Na_5[Al_5Si_5O_{20}]\cdot 9H_2O$ and Ba-zeolite edingtonite (ICSD 29516, chemical composition $Ba_2[Al_4Si_6O_{20}]\cdot 6.92H_2O$). It is clear that the distortion of the 8M ring increases in the order zeolite F → MMU-1 → edingtonite, which correlates with the increase in the average ionic radius of the cationic modifiers. It should be underlined that the framework topology of MMU-1 resembles that of edingtonite, as can be best viewed normally to the *c* axis (Figure 10): the central tetrahedral position in edingtonite (Si1) (Figure 10b) is nonequivalent in alternating layers of MMU-1 along the tetragonal [001] direction, resulting in a doubling of the *c* axis and positions T3 and T4 in the MMU-1 structure (Figure 10a). Additionally, the TO_4 framework of edingtonite is rotated about the *c* axis by approximately 20° (Figure 10c).

4. CONCLUSIONS

Nanosized zeolites RHO and a new zeolite MMU-1 of EDI framework topology type were prepared from precursor solutions with the molar compositions of 10 SiO_2:0.77 Al_2O_3:7.9 Na_2O:0.47 Cs_2O:110 H_2O and 10 SiO_2:2.2 Al_2O_3:23 Na_2O:1.4 Cs_2O:383 H_2O, respectively. The presence of both cesium hydroxide and a certain level of water was crucial for the type of zeolite formed. Cancrinite was formed when the water in the latter molar composition was decreased from 383 to 294. Cancrinite was also crystallized from the solvent-free synthesis employing a mixture with the molar composition of 10 SiO_2:0.77 Al_2O_3:7.9 Na_2O:0.47 Cs_2O:2 H_2O (traces of water from the use of $CsOH\cdot xH_2O$), further confirming the crucial role of water. The structural changes between the zeolite precursors and zeolites formed were followed by Raman and FTIR spectroscopy, which revealed changes in the intermediate-range order upon hydrothermal treatment (water-mediated synthesis) and heat treatment (solvent-free synthesis).

The structure of the new zeolite MMU-1 was resolved by Rietveld refinement. MMU-1 was found to exhibit tetragonal symmetry, space group $P\bar{4}2_1c$ (No. 114), with four-membered and eight-membered TO_4-rings and with a nominal chemical formula of $(Cs_{1.17}Na_{3.69})[Si_{5.14}Al_{4.86}O_{20}]\cdot 7H_2O$. The results reported in this work suggest that there is potential to synthesize other novel eight-membered zeolite structures in the presence of cesium hydroxide by modifications in the chemical

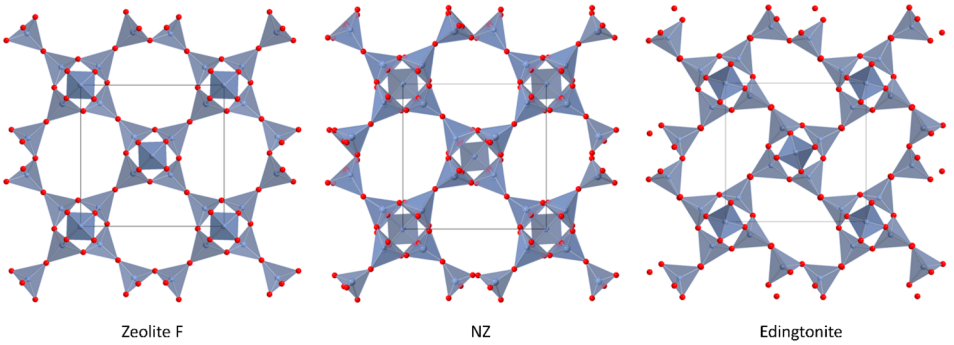

Figure 9. Structural fragments of zeolite F (ICSD 6772), NZ (this study), and edingtonite (ICSD 29516) projected along the tetragonal [001] direction.

https://doi.org/10.1021/acs.cgd.3c00239
Cryst. Growth Des. 2023, 23, 3834−3844

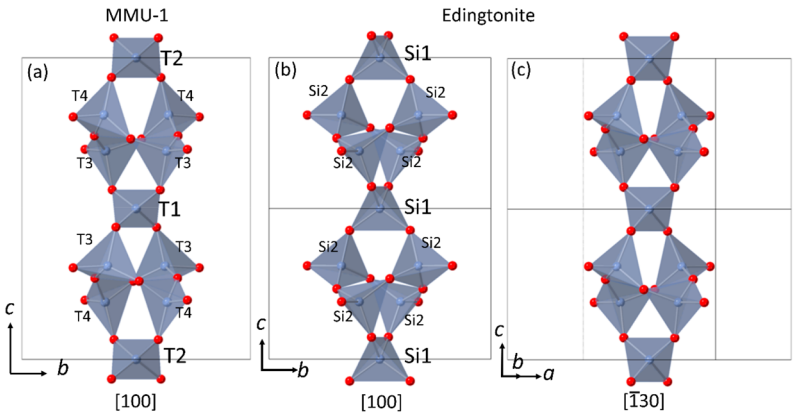

Figure 10. Comparison between the 4-fold-ring framework topologies of (a) MMU-1 and (b) edingtonite viewed along [100]; (c) shows edingtonite along [$\bar{1}$30]. The structure of edingtonite is presented with an origin shifted to (0.5, 0.5, 0).

composition of the zeolite precursor solutions. Such zeolites are of interest for commercial applications such as NO_x removal, catalytic conversion of methanol to light olefins, and CO_2 capture and separation technologies.

■ ASSOCIATED CONTENT

Supporting Information

The Supporting Information is available free of charge at The Supporting Information is available free of charge at https://pubs.acs.org/doi/10.1021/acs.cgd.3c00239.

Adsorption isotherms and an SEM image of the cancrinite sample prepared from solution C, comparison between the MMU-1 samples prepared with different silica sources (XRD patterns, adsorption isotherms, and SEM images), and details of the atomic-structure refinement of MMU-1 (PDF)

Accession Codes

CCDC 2246630 contains the supplementary crystallographic data for this paper. These data can be obtained free of charge via www.ccdc.cam.ac.uk/data_request/cif, or by emailing data_request@ccdc.cam.ac.uk, or by contacting The Cambridge Crystallographic Data Centre, 12 Union Road, Cambridge CB2 1EZ, UK; fax: +44 1223 336033.

■ AUTHOR INFORMATION

Corresponding Author

Lubomira Tosheva − *Faculty of Science and Engineering, Manchester Metropolitan University, Manchester M1 5GD, United Kingdom;* orcid.org/0000-0002-3605-9851; Email: l.tosheva@mmu.ac.uk

Authors

Krassimir Garbev − *Department of Technical Mineralogy, Institute for Technical Chemistry, Karlsruhe Institute of Technology, 76021 Karlsruhe, Germany;* orcid.org/0000-0002-3303-5168

Gary J. Miller − *Faculty of Science and Engineering, Manchester Metropolitan University, Manchester M1 5GD, United Kingdom*

Boriana Mihailova − *Mineralogisch-Petrographisches Institut, FB Erdsystemwissenschaften, Universität Hamburg, 20146 Hamburg, Germany;* orcid.org/0000-0003-0504-7521

Complete contact information is available at: https://pubs.acs.org/10.1021/acs.cgd.3c00239

Author Contributions

The manuscript was written through contributions of all authors. All authors have given approval to the final version of the manuscript.

Notes

The authors declare no competing financial interest.

■ ACKNOWLEDGMENTS

This work was supported by The Royal Society, UK, IEC \NSFC\211137. We thank Prof. Roger Rothon for providing us with the Geo40 sol-UF2 silica sol.

■ REFERENCES

(1) Ng, E.-P.; Chateigner, D.; Bein, T.; Valtchev, V.; Mintova, S. Capturing Ultrasmall EMT Zeolite from Template-Free Systems. *Science* **2012**, *335*, 70−73.

(2) Awala, H.; Gilson, J.-P.; Retoux, R.; Boullay, P.; Goupil, J.-M.; Valtchev, V.; Mintova, S. Template-free Nanosized Faujasite-type Zeolites. *Nat. Mater.* **2015**, *14*, 447−451.

(3) Zhang, C.; Wu, Q.; Lei, C.; Han, S.; Zhu, Q.; Maurer, S.; Dai, D.; Parvulescu, A.-N.; Ulrich Muller, U.; Meng, X.; Xiao, F.-S. An Efficient, Rapid, and Non-centrifugation Synthesis of Nanosized Zeolites by Accelerating the Nucleation Rate. *J. Mater. Chem. A* **2018**, *6*, 21156−21161.

(4) Wu, Q. M.; Meng, X. J.; Gao, X. H.; Xiao, F. S. Solvent-Free Synthesis of Zeolites: Mechanism and Utility. *Acc. Chem. Res.* **2018**, *51* (6), 1396−1403.

(5) Joseph, I. V.; Doyle, A. M.; Amedlous, A.; Mintova, S.; Tosheva, L. Scalable Solvent-free Synthesis of Aggregated Nanosized Single-Phase Cancrinite Zeolite. *Mater. Today Commun.* **2022**, *32*, 103879.

(6) Chen, X.; Yang, G.; Valtchev, V. Environmentally Benign Synthesis of Crystalline Nanosized Molecular Sieves. *Green Energy Environ.* **2020**, *5*, 394−404.

(7) Dusselier, M.; Davis, M. E. Small-Pore Zeolites: Synthesis and Catalysis. *Chem. Rev.* **2018**, *118*, 5265−5329.

(8) Zanco, S. E.; Pérez-Calvo, J.-F.; Gasós, A.; Cordiano, B.; Becattini, V.; Mazzotti, M. Postcombustion CO_2 Capture: A Comparative Techno-Economic Assessment of Three Technologies Using a Solvent, an Adsorbent, and a Membrane. *ACS Eng. Au* **2021**, *1* (1), 50−72.

(9) Palomino, M.; Corma, A.; Jordá, J. L.; Rey, F.; Valencia, S. Zeolite Rho: a Highly Selective Adsorbent for CO_2/CH_4 Separation Induced by a Structural Phase Modification. *Chem. Commun.* **2012**, *48*, 215−217.

(10) Coudert, F.-X.; Kohen, D. Molecular Insight into CO2 "Trapdoor" Adsorption in Zeolite Na-RHO. *Chem. Mater.* **2017**, *29*, 2724−2730.

(11) Liang, D.; Hu, Y.; Bao, Q.; Zhang, J.; Feng, J.; Sun, P.; Ma, Y.; Zhang, H. A Suitable Zeolite Rho for Separating CO_2/CH_4 in Pressure Swing Adsorption (PSA) Process. *Inorg. Chem. Commun.* **2021**, *127*, 108547.
(12) Lozinska, M. M.; Jamieson, S.; Verbraeken, M. C.; Miller, D. N.; Bode, B. E.; Murray, C. A.; Brandani, S.; Wright, P. A. Cation Ordering and Exsolution in Copper-Containing Forms of the Flexible Zeolite Rho (Cu,M-Rho; M = H, Na) and Their Consequences for CO2 Adsorption. *Chem. - Eur. J.* **2021**, *27*, 13029−13039.
(13) Belani, M. R.; Somani, R. S.; Bajaj, H. C. Sorption of Carbon Dioxide, Methane, and Nitrogen on Zeolite-F: Equilibrium Adsorption Study. *Environ. Prog. Sustain. Energy* **2017**, *36* (3), 850.
(14) Choi, H. J.; Jo, D.; Min, J. G.; Hong, S. B. The Origin of Selective Adsorption of CO_2 on Merlinoite Zeolites. *Angew. Chem., Int. Ed.* **2021**, *60*, 4307−4314.
(15) Choi, H. J.; Hong, S. B. Effect of Framework Si/Al Ratio on the Mechanism of CO2 Adsorption on the Small-Pore Zeolite Gismondine. *Chem. Eng. J.* **2022**, *433*, 133800.
(16) Grand, J.; Barrier, N.; Debost, M.; Clatworthy, E. B.; Laine, F.; Boullay, P.; Nesterenko, N.; Dath, J.-P.; Gilson, J.-P.; Mintova, S. Flexible Template-Free RHO Nanosized Zeolite for Selective CO_2 Adsorption. *Chem. Mater.* **2020**, *32*, 5985−5993.
(17) Confalonieri, G.; Grand, J.; Arletti, R.; Barrier, N.; Mintova, S. CO_2 Adsorption in Nanosized RHO Zeolites with Different Chemical Compositions and Crystallite Sizes. *Microporous Mesoporous Mater.* **2020**, *306*, 110394.
(18) Grazulis, S.; Chateigner, D.; Downs, R. T.; Yokochi, A. T.; Quiros, M.; Lutterotti, L.; Manakova, E.; Butkus, J.; Moeck, P.; Le Bail, A. Crystallography Open Database - an Open-Access Collection of Crystal Structures. *J. Appl. Crystallogr.* **2009**, *42*, 726−729.
(19) Maldonado, M.; Oleksiak, M. D.; Chinta, S.; Rimer, J. D. Controlling Crystal Polymorphism in Organic-Free Synthesis of Na-Zeolites. *J. Am. Chem. Soc.* **2013**, *135*, 2641−2652.
(20) Roozeboom, F.; Robson, H. E.; Chan, S. S. Laser Raman Study on the Crystallization of Zeolites A, X and Y. *Zeolites* **1983**, *3*, 321−328.
(21) Matson, D. W.; Sharma, S. K.; Philpotts, J. A. Raman Spectra of Some Tectosilicates and of Glasses along the Orthoclase-anorthite and Nepheline-anorthite Joins. *Am. Mineral.* **1986**, *71*, 694−704.
(22) Wang, T.; Luo, S.; Tompsett, G. A.; Timko, M. T.; Fan, W.; Auerbach, S. M. Critical Role of Tricyclic Bridges Including Neighboring Rings for Understanding Raman Spectra of Zeolites. *J. Am. Chem. Soc.* **2019**, *141* (51), 20318−20324.
(23) Kosorukov, A. A.; Nadel, L. K-F Zeolite and its Rubidium and Caesium analogues. *Russ. J. Inorg. Chem.* **1985**, *30*, 961−963.
(24) Baerlocher, C. H.; Barker, R. M. The Crystal Structure of Synthetic Zeolite F. *Z. Kristallogr. Cryst. Mater.* **1974**, *140* (1−2), 10−26.
(25) Coelho, A. A. A Charge Flipping Algorithm Incorporating the Tangent Formula for Solving Difficult Structures. *Acta Crystallogr.* **2007**, *63*, 400−406.
(26) Kwon, S.; Kim, C.; Han, E.; Lee, H.; Cho, H. S.; Choi, M. Relationship between Zeolite Structure and Capture Capability for Radioactive Cesium and Strontium. *J. Hazard. Mater.* **2021**, *408* (2021), 124419.
(27) Parise, J. B.; Prince, E. The Structure of Cesium-exchanged Zeolite-RhO at 293K and 493K Determined from High Resolution Neutron Powder Data. *Mater. Res. Bull.* **1983**, *18* (7), 841−852.

https://doi.org/10.1021/acs.cgd.3c00239
Cryst. Growth Des. 2023, 23, 3834−3844